Analysis of thermal stress, fatigue life and allowable flux density for the molten salt receiver in solar power tower plants

Yan Luo[1,*], Gen Li[1], Tao Lu[1] and Ruixing Wang[2,3,*]

[1]*School of Mechanical and Electrical Engineering, Beijing University of Chemical Technology, Beijing 100029, China;* [2]*Key Laboratory for Mechanics in Fluid–Solid Coupling Systems, Institute of Mechanics, Chinese Academy of Sciences, Beijing 100190, China;* [3]*School of Engineering Sciences, University of Chinese Academy of Sciences, Beijing 100049, China*

Abstract

The solar power tower (SPT) receiver design should be able to stand with fatigue damage caused by the passage of clouds, start-up and shut-down. In this paper, to investigate the impacts of incident heat flux distribution and SPT site weather data on the thermal stress, fatigue life and allowable flux density (AFD) of the molten salt receiver, the relationship between the fatigue life and AFD of the tube wall is developed based on the coupled thermal–structural analysis and Miner linear damage theory. The results show that the cosine effect of the circumferential heat flux distribution considered has a significant influence on the location and magnitude of the maximum thermal stress of the tube wall, which lead to the difference in the tube wall fatigue damage. The AFD are, respectively, 829 kW/m^2 and 1037 kW/m^2 under uniform and cosine circumferential heat flux distributions for the site of Barstow, USA, when the design lifetime of the tube is 30 years. Compared with the SPT site of Barstow, USA, the fatigue damage of the tube wall in Sevilla, Spain, and Delingha, China, are lower under the same conditions due to lower insolation hours of direct normal irradiation in the range of 750–1100 W/m^2. The AFD are, respectively, 829 kW/m^2, 973 kW/m^2 and 997 kW/m^2 for the site of Barstow, USA, Sevilla, Spain, and Delingha, China, with 30 years design life. These findings give guidelines for the operation reliability of the SPT molten salt receiver tube.

Keywords: local weather data; incident heat flux distribution; allowable flux density; fatigue life analysis; solar power tower receiver

*Corresponding author:
luoyan@mail.buct.edu.cn
(Y. Luo);
wangruixing@imech.ac.cn
(R. Wang)

1 INTRODUCTION

Among different concentrated solar power technologies, the solar power tower (SPT) system has the advantages of large-scale utilization and low cost, which concentrates the sunlight onto a receiver mounted at the top of a tower. The solar receiver is an important component in the solar power generation system and needs to stand with fatigue damage, which is caused by repeatedly changed thermal stress due to the passage of clouds, start-up and shut-down [1]. To guarantee the operation safety of the receiver, it is necessary to conduct thermal stress and fatigue analysis of the receiver tube wall.

Thermal stress distribution of the receiver tube wall is the basis to conduct fatigue analysis. Recently, numerous researchers applied different theoretical equations to evaluate the thermal stress based on the temperature distribution of the receiver. Sánchez-González *et al.* [2, 3], Rodríguez-Sánchez *et al.* [4] and Nithyanandam *et al.* [5] utilized theoretical equations presented by Young *et al.* [6] and Timošenko [7] to calculate the thermal stress of the solar receiver tube wall by accounting for only

the radial temperature gradient ($\sigma \propto T(r)$). Kim et al. [8] and Conroy et al. [9] evaluated the thermal stress of the solar receiver tube wall by superimposing contributions of both radial and circumferential temperature gradient ($\sigma \propto T(r, \theta)$). As a result, due to the omission of axial or circumferential temperature gradient, the above simplified theoretical equations may not be accurate enough for complex boundary conditions encountered on solar receiver tube. To obtain the actual stress distribution of the receiver tube wall, the finite element method (FEM) is recently chosen by some researchers [10–16]. Ortega et al. [10] adopted the FEM to obtain radial, circumferential and axial stresses throughout the supercritical carbon dioxide receiver tube by coupling ANSYS Fluent with ANSYS Structural. Wan et al. [11] also applied similar methodology for comprehension evaluation of thermal stress distribution on the receiver tube wall.

Once the thermal stress distribution of the solar receiver tube wall is acquired, the fatigue damage of the solar receiver tube caused by frequent changed thermal stress is investigated [5, 17–19]. Narayanan et al. [17] assumed 11 000 diurnal and 19 000 cloud thermal cycles of the same severity for the receiver design lifetime of 30 years. Then the linear damage rule was adopted to calculate the fatigue damage of the receiver, which was the ratio of the actual thermal cycles and the corresponding allowable fatigue cycles to the equivalent thermal stress magnitude. Chen et al. [18] also obtained the fatigue damage of the receiver by the linear damage rule. The actual thermal cycle number in the design life was set as 10 000 under design point load and the allowable thermal cycle number was decided by the equivalent thermal stress. As a whole, the linear damage rule is applied to obtain the fatigue damage of the receiver, which is usually determined by the equivalent thermal stress.

Actually, to guide the design of the receiver, the fatigue damage limitation of the receiver is always translated into the allowable flux density (AFD) incident on the receiver, which is directly related to the thermal stress of the tube wall. Vant-Hull [20] calculated the AFD of a molten salt receiver for fatigue life of 30 years with the limitation of the allowable equivalent thermal stress, which corresponded to the 40 000 thermal cycles. It demonstrated that the AFD of the receiver is 850 kW/m^2 at the 561 K inlet salt temperature. Liao et al. [21] adopted the corresponding allowable thermal stress to 36 000 fatigue cycles as limiting function for fatigue to calculate the AFD. The result showed that the AFD could reach 0.88 MW/m^2 with the 316ss tube material for the molten salt receiver. Luo et al. [22] applied a similar limit to that of Liao et al. [21] to determine the AFD of a direct steam receiver under different conditions of velocities, tube diameters and steam pressure. It should be noted that the above literatures assumed that the thermal stress magnitude remained unchanged during thermal cycling. However, Kistler [23] pointed out that the stress cycles experienced by the solar receiver varied in magnitude because the solar irradiation density changed each day and each cloud passage was different. Therefore, the previous models that established the relationship between the AFD and fatigue life were not accurate enough and the actual SPT site weather data should be used to determine the fatigue life and AFD. Besides, the
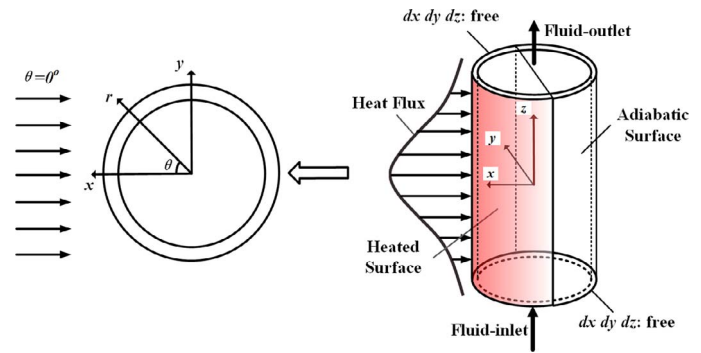

Figure 1. *Physical model of the solar receiver tube.*

Table 1. *Properties of molten salt.*

Properties	Correlations with T (K)
Destiny ρ (kg/m^3)	$\rho = 2090 - 0.636 \times (T - 273.15)$
Specific heat c_p (J/(kg·K))	$c_p = 1443 + 0.172 \times (T - 273.15)$
Viscosity μ (Pa·s)	$\mu = (22.714 - 0.12 \times (T - 273.15) + 2.281 \times 10^{-4} \times (T - 273.15)^2 - 1.474 \times 10^{-7} \times (T - 273.15)^3) \times 10^{-3}$
Thermal conductivity λ (W/m·K)	$\lambda = 0.443 + 1.9 \times 10^{-4} \times (T - 273.15)$

previous AFD calculation models were generally simplified to a one-dimensional radial heat transfer process, resulting in that the changes in the axial and circumferential incident solar heat flux were ignored. In this regard, the effects of the SPT site weather data and incident solar heat flux distribution on the fatigue life and AFD of the receiver tube should be clarified.

The main goal of the present work is to investigate the influences of the incident heat flux distribution and SPT site weather data on the thermal stress, fatigue life and AFD of the SPT molten salt receiver tube, thus providing more accurate guidelines for the safe operation of solar receiver. For the purpose, a coupled thermal–structural analysis is conducted by importing the inner and outer tube wall temperature distributions from the finite volume method (FVM) simulation to the FEM calculation. Based on the time-varying thermal stress of the tube wall, the fatigue life analysis is then performed by combining the rain flow counting method and the Miner linear damage rule, allowing us to determine the optimal AFD under different incident heat flux distributions and different SPT site weather data. The results are beneficial to increase the operation reliability of the SPT molten salt receiver tube.

2 METHODOLOGY

2.1 Physical model
Physical model of the solar receiver tube for the molten salt SPT plant system is shown in Figure 1. The length and inner/outer radius of the solar receiver tube are 3 m and 10.5/12.5 mm,
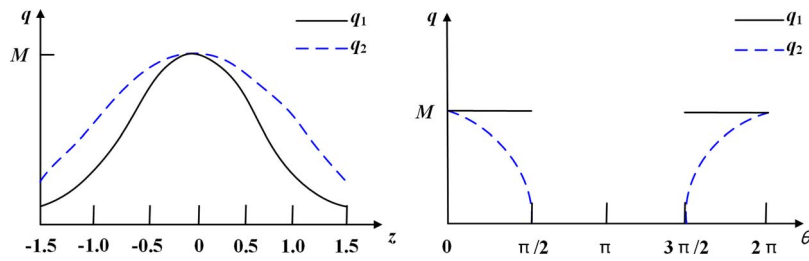
Figure 2. *Two incident heat flux distributions. (a) Axial heat flux distribution; (b) circumferential heat flux distribution.*
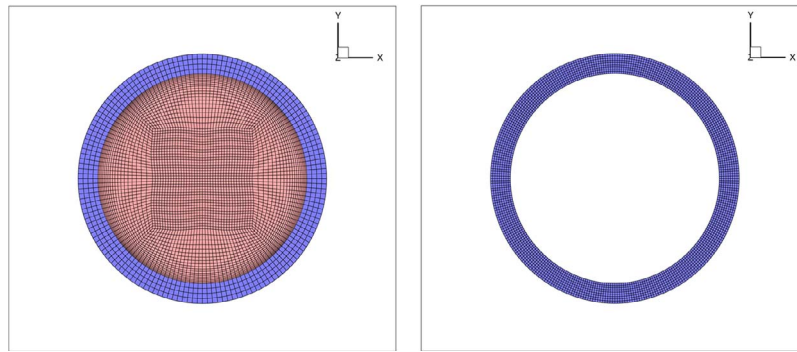

Figure 3. *Computation meshes for the temperature and thermal stress analysis. (a) Meshes for FVM analysis; (b) finer meshes for FEM analysis.*

Table 2. *Properties of 316H stainless steel.*

Properties	Values
Destiny ρ (kg/m³)	7090
Specific heat c_p (J/(kg·K))	500
Thermal conductivity λ (W/m·K)	21.5
Poisson's ratio ν	0.3
Thermal expansion coefficient α (1/K)	$\alpha = 1.43 \times 10^{-5} + 7.34 \times 10^{-9}T - 2.65 \times 10^{-12}T^2$
Elastic modulus E (Pa)	$E = 2.11 \times 10^{11} - 3.59 \times 10^7 T - 3.75 \times 10^4 T^2$

respectively. The receiver operates in the mode of rated mass flow, and the inlet velocity is fixed at 3 m/s. The heat transfer fluid is molten nitrate salt (60% $NaNO_3$ + 40%KNO_3) with inlet temperature of 673 K, and its properties are given in Table 1 [24]. The tube material is 316H stainless steel and the properties for the material can be seen in Table 2 [1].

As shown in Figure 1, the solar receiver tube is subjected to non-uniform and time-varying heat flux, which may induce high thermal stress and fatigue damage. At present, some researchers have studied the axial and circumferential heat flux distributions on the receiver tube. Boerema *et al.* [25], Marocco *et al.* [26], Liu *et al.* [27] and Fang *et al.* [28] approximated the axial and circumferential heat flux to normal and cosine distribution, respectively. Du *et al.* [1] and Wang *et al.* [29] assumed that the heat flux along axial direction obeyed normal distribution and the circumferential heat flux distribution of the heated surface is uniform. In conclusion, the axial heat flux distribution is generally approximated by a normal distribution and the circumferential heat flux distribution is often modeled with a cosine or uniform function. Therefore, in this paper, two incident heat flux distributions are considered and shown in Figure 2. The two incident heat flux distributions can be, respectively, expressed as

$$q_1 = \begin{cases} M\,e^{-1.33z^2} & \cos\theta \geq 0 \\ 0 & \cos\theta < 0 \end{cases} \tag{1}$$

$$q_2 = \begin{cases} M\,e^{-0.34z^2}\,\cos\theta & \cos\theta \geq 0 \\ 0 & \cos\theta < 0 \end{cases} \tag{2}$$

where M is the peak heat flux imposed on the receiver tube wall, θ and z are described in Figure 1. q_1 and q_2 represent that the circumferential heat flux distributions are, respectively, modeled with a uniform and cosine function. Although the axial heat flux distributions for q_1 and q_2 are both normal, parameters of the two normal distributions are different to ensure that the total heat fluxes on the tube wall are identical.

2.2 Temperature analysis

In the temperature analysis, the molten salt flow and heat transfer are assumed in a steady and thermal equilibrium state. The convection heat transfer and thermal radiation between the outer tube wall and air are neglected. The governing equations of molten salt flow inside the solar receiver tube consist of continuity, momentum and energy equations [30]. The standard k-ε model is adopted for turbulent flow simulation [30]. The inlet and outlet boundary conditions of the receiver tube are, respectively, velocity
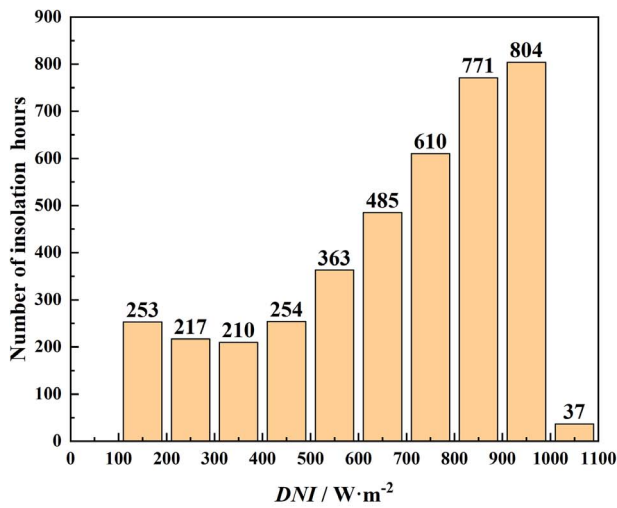
(a)
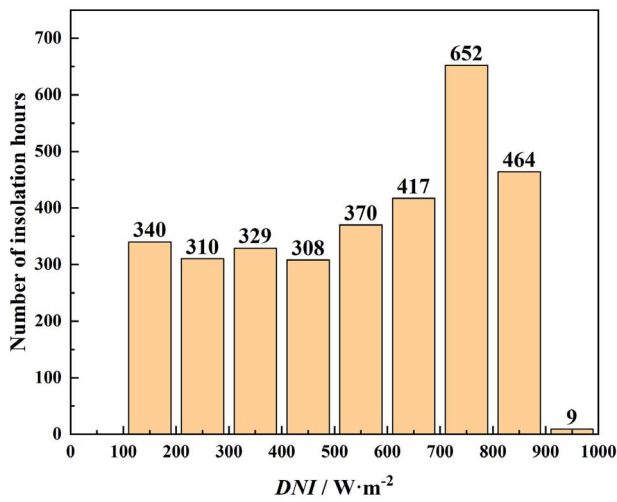
(b)
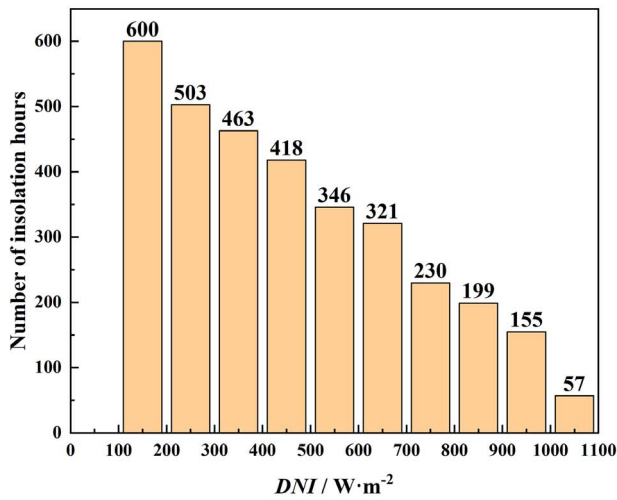
(c)

Figure 4. *Variations of insolation hours with DNI ranges for a typical meteo-rological year at these three locations. (a) Barstow, USA; (b) Sevilla, Spain; (c) Delingha, China.*
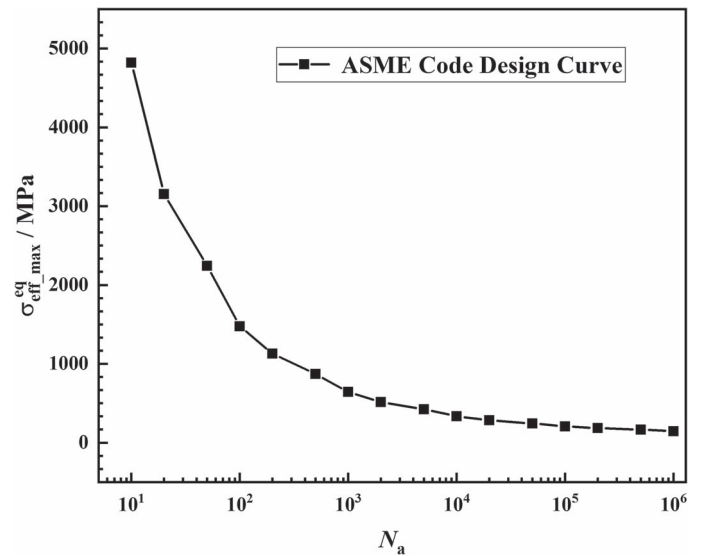

Figure 5. *S-N curve of 316H stainless steel at a temperature of 540–650°C.*

inlet and pressure outlet. The non-uniform heat flux is imposed on the receiver tube outer wall by using user-defined functions.

The governing equations of the molten salt flow and heat transfer are solved by the FVM simulation with Fluent 2022R1 software. The second-order scheme is used to discretize the equations. The SIMPLE algorithm is used for the pressure–velocity coupling. Grid independence has been tested. It is found that 45 296 grid elements in solid part and 322 734 grid elements in fluid part are adequate as shown in Figure 3a.

2.3 Thermal stress analysis

The coupled thermal–structural analysis is conducted by sequentially coupling method due to high computational efficiency and negligible influence of thermal stress distribution on the temperature distribution. In the thermal stress analysis, the inner and outer tube wall temperature distributions are interpolated to the nodes of the thermal stress analysis meshes. As shown in Figure 3b, a finer solid part with 209 196 grid elements is used to obtain more accurate results.

The heat transfer and thermoelasticity of the tube wall are obtained by the FEM simulation with Abaqus software. In this paper, the receiver tube is unrestrained at both ends. Consequently, the thermal stress of the tube wall is caused by the coupling of the temperature gradient and solid structure. According to the Von-Mises theory, the expression of effective thermal stress equation in the form of cylindrical coordinates is shown as follows [31]:

$$\sigma_{\text{eff}} = \sqrt{\sigma_z^2 + \sigma_r^2 + \sigma_\theta^2 - \left(\sigma_z\sigma_r + \sigma_r\sigma_\theta + \sigma_\theta\sigma_z\right)} \quad (3)$$

where $\sigma_z, \sigma_r, \sigma_\theta$ are thermal stresses in the axial, radial and circumferential direction, respectively.
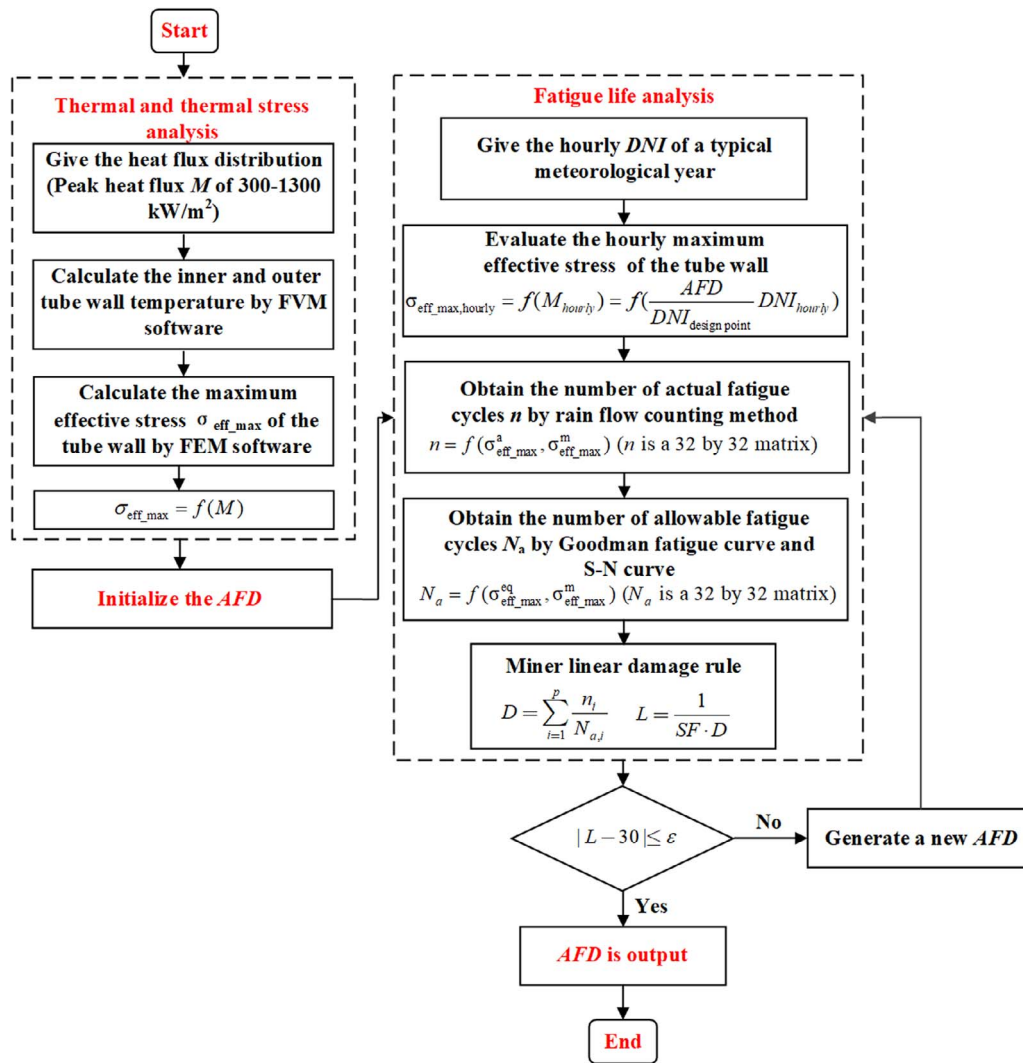
Figure 6. *Flowchart of the determination of AFD for the receiver.*

2.4 Fatigue life analysis

The frequent changed thermal stress would lead to fatigue and creep damage of the solar receiver tube due to the passage of clouds, start-up and shut-down. Some researchers [32, 33] considered fatigue damage as well as creep damage for mechanical reliability estimation of receivers using high pressure and temperature working fluid, such as supercritical carbon dioxide. However, Kistles [23] and Kolb [34] pointed out that the creep damage could be ignored because of small pressure and relative low temperature of the molten salt receiver tube. Consequently, in this paper, it may be justified to only include the fatigue damage calculation for the mechanical reliability analysis of the molten salt receiver.

Conservative estimation of the receiver fatigue life is performed based on the time-varying maximum effective thermal stress of the receiver tube wall. Three different locations of the incident direct normal irradiation (DNI) are given for fatigue life analysis: Barstow (34.85°N, −116.8°W), USA; Sevilla (37.4°N, 5.9°W), Spain; Delingha (37.37°N, 97.37°W), China. The hourly DNI

of these three sites can be obtained from the System Advisor Model software [35], which contains typical-year meteorological data that represent long-term historical data. The annual DNI for the sites of Barstow, Sevilla and Delingha are 2723 kWh/m², 1773 kWh/m² and 1544 kWh/m², respectively. Figure 4 gives variations of insolation hours with DNI ranges for a typical meteorological year at these three locations. It can be seen that most of the insolation hours are in the ranges of high DNI for the site of Barstow, while the opposite tendency for the site of Delingha. The differences in insolation hours for different DNI ranges are not significant at the location of Sevilla.

To conduct fatigue life analysis, the heliostat field efficiency and the receiver efficiency are assumed constant for two reasons. One reason is that the optical efficiency of the heliostat field and the thermal efficiency of the receiver change slightly when the DNI is larger than 400 W/m² [36]. Another reason is that no fatigue damage occurs on the tube wall when the DNI is small. Therefore, the ratio of the hourly peak heat flux on the receiver tube wall to
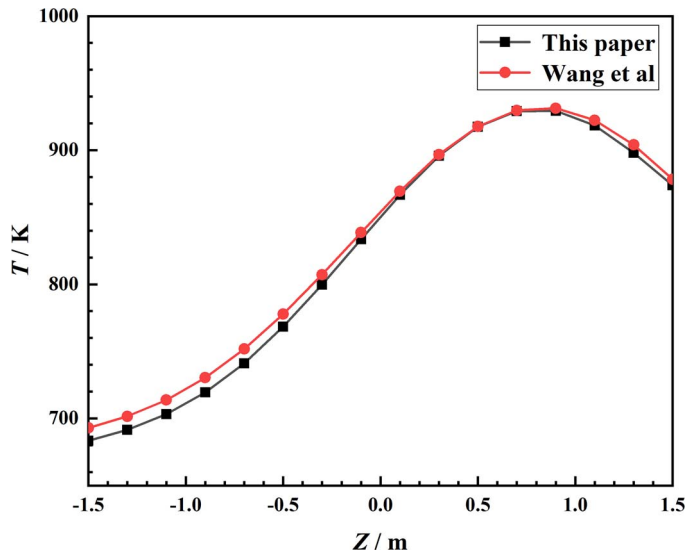
Figure 7. *Comparison of temperature distribution of the tube wall with the result of Wang et al.*

Figure 8. *Comparison of thermal stress distribution of the tube wall with the analytical result.*

the hourly DNI of a typical meteorological year can be considered as constant under the condition that the heliostat aiming strategy is fixed. As the receiver design satisfies the AFD constraint at the design point, the hourly peak heat flux M_{hourly} can be calculated as follows:

$$M_{\text{hourly}} = \frac{AFD}{DNI_{\text{design point}}} DNI_{\text{hourly}} \qquad (4)$$

where $DNI_{\text{design point}}$ is the DNI value at design point.

Based on the hourly peak heat flux M_{hourly} on the receiver tube surface, the hourly maximum effective thermal stress $\sigma_{\text{eff\_max,hourly}}$ of the tube wall can be obtained by the method described in Sections 2.2 and 2.3. To conduct fatigue life analysis, the rain flow counting method [37] is applied to convert the hourly maximum thermal stress into a rain flow matrix, which represents the number of actual fatigue cycles n under different stress amplitude $\sigma_{\text{eff\_max}}^{a}$ and mean stress $\sigma_{\text{eff\_max}}^{m}$. To inspect the convergence of the results obtained by the rain flow counting method, rain flow matrix dimensions of 16 by 16, 32 by 32 and 64 by 64 are all employed. The results show that the rain flow counting method approached the equilibrium statues for the rain flow matrix dimension of 32 by 32. Therefore, the rain flow matrix dimension of 32 by 32 is applied in this paper. The expressions of $\sigma_{\text{eff\_max}}^{a}$ and $\sigma_{\text{eff\_max}}^{m}$ are as follows:

$$\sigma_{\text{eff\_max}}^{a} = \frac{\sigma_{\text{eff\_max}}^{\text{cmax}} - \sigma_{\text{eff\_max}}^{\text{cmin}}}{2} \qquad (5)$$

$$\sigma_{\text{eff\_max}}^{m} = \frac{\sigma_{\text{eff\_max}}^{\text{cmax}} + \sigma_{\text{eff\_max}}^{\text{cmin}}}{2} \qquad (6)$$
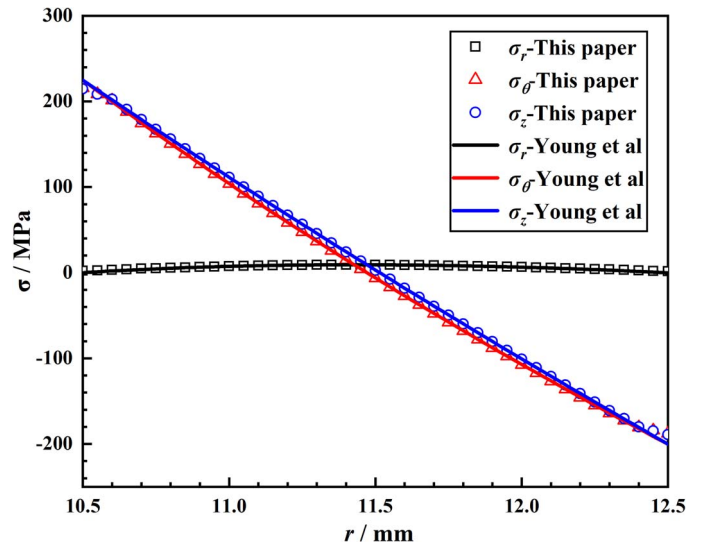
where $\sigma_{\text{eff\_max}}^{\text{cmax}}$ and $\sigma_{\text{eff\_max}}^{\text{cmin}}$ are, respectively, maximum and minimum thermal stresses in a thermal stress cycle.

In general, the S-N curve of tube material is obtained by experiments under symmetrical cyclic load. However, the thermal stress cyclic load of the tube wall is asymmetric. Therefore, the stress amplitude $\sigma_{\text{eff\_max}}^{a}$ under different mean stress $\sigma_{\text{eff\_max}}^{m}$ should be converted into the equivalent stress amplitude $\sigma_{\text{eff\_max}}^{\text{eq}}$ under mean stress of 0. The Goodman mean stress correction curve is applied and expressed as [38],

$$\frac{\sigma_{\text{eff\_max}}^{a}}{\sigma_{\text{eff\_max}}^{\text{eq}}} + \frac{\sigma_{\text{eff\_max}}^{m}}{\sigma_{u}} = 1 \qquad (7)$$

where σ_{u} is the tensile strength of the tube material.

The S-N curve of 316H stainless steel at temperature of 540–650°C is shown in Figure 5, which is given in the ASME Boiler and Pressure Vessel code [39]. It should be noted that no fatigue damage occurs on the tube wall when the equivalent stress amplitude $\sigma_{\text{eff\_max}}^{\text{eq}}$ is lower than 146 MPa. Based on the S-N curve of 316H stainless steel, the number of allowable fatigue cycles N_{a} under different equivalent stress amplitude $\sigma_{\text{eff\_max}}^{\text{eq}}$ is obtained. The yearly cumulative fatigue damage D resulting from these cycles can be calculated by the Miner linear damage rule and expressed as follows [40],

$$D = \sum_{i=1}^{p} \frac{n_i}{N_{a,i}} \qquad (8)$$

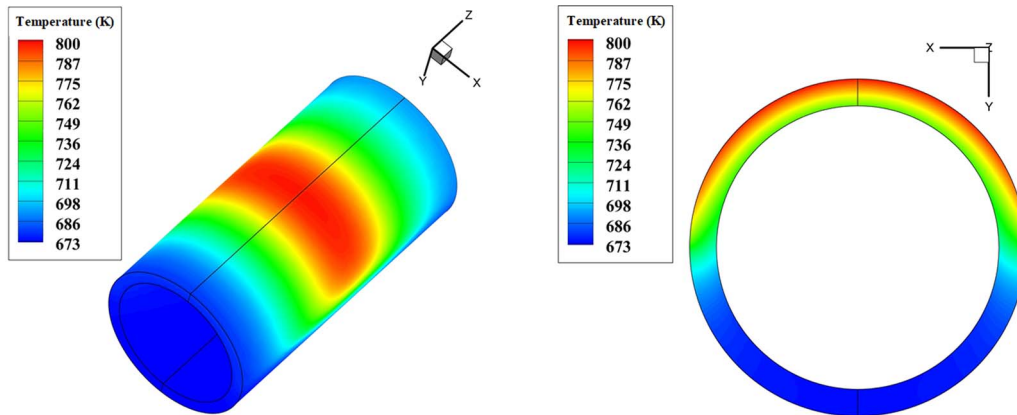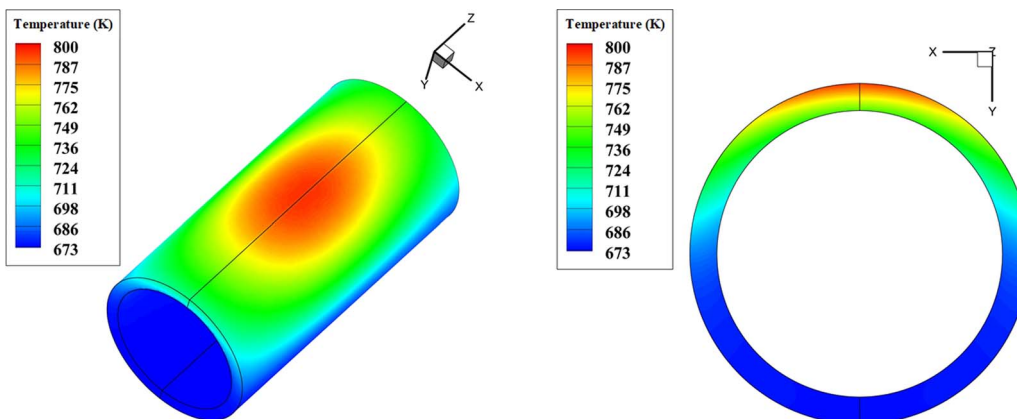where p is the number of elements in the rain flow matrix (32 by 32).

Figure 9. *Temperature distribution of the tube wall under heat flux distribution of Eq. (1) with peak heat flux M of 500 kW/m². (a) Whole tube wall (z = 1:60); (b) cross-wall of the tube (z = 0 m).*

Figure 10. *Temperature distribution of the tube wall under heat flux distribution of Eq. (2) with peak heat flux M of 500 kW/m². (a) Whole tube wall (z = 1:60); (b) cross-wall of the tube (z = 0 m).*

Based on the yearly cumulative fatigue damage, the fatigue life L of the tube can be obtained and expressed as,

$$L = \frac{1}{SF \cdot D} \qquad (9)$$

where SF represents the safety factor of fatigue life and is generally set as 2 [23]. Considering that the design lifetime of solar receiver is generally 30 years, the receiver tube design should satisfy | L − 30 |≤ ε.

2.5 Determination of AFD

AFD is a significant parameter for the fatigue life of the receiver since it is directly related to the hourly peak heat flux on the receiver tube wall. Figure 6 illustrates a flowchart of the determination of AFD for the receiver. The detailed strategy procedure is given as follows:

1) **Conduct the thermal and thermal stress analysis.** Based on the given heat flux distribution, the receiver tube wall temperature distributions are calculated by FVM software with variation of peak heat flux from 300 kW/m² to 1100 kW/m². Then the inner and outer tube wall temperatures are interpolated to conduct thermal stress analysis by FEM software. Consequently, the relationship between the peak heat flux M and the maximum effective thermal stress $\sigma_{\text{eff\_max}}$ of the tube wall can be developed and expressed as $\sigma_{\text{eff\_max}} = f(M)$.

2) **Initialize the AFD.** The AFD constraint of the receiver at the design point is assigned randomly.

3) **Obtain the hourly maximum thermal stress.** Based on the AFD constraint and the hourly DNI of a typical meteorological year, the hourly peak heat flux is calculated according to the Eq. (4). Then the hourly maximum thermal stress on the tube wall is evaluated by the expression of $\sigma_{\text{eff\_max}} = f(M)$.

4) **Conduct the fatigue life analysis.** The rain flow counting method is used to convert the hourly maximum thermal stress into the number of actual fatigue cycles n under different stress amplitude $\sigma_{\text{eff\_max}}^{\text{a}}$ and mean stress $\sigma_{\text{eff\_max}}^{\text{m}}$. The Goodman fatigue curve and S-N curve are applied to calculate the number of allowable fatigue cycles N_a under different

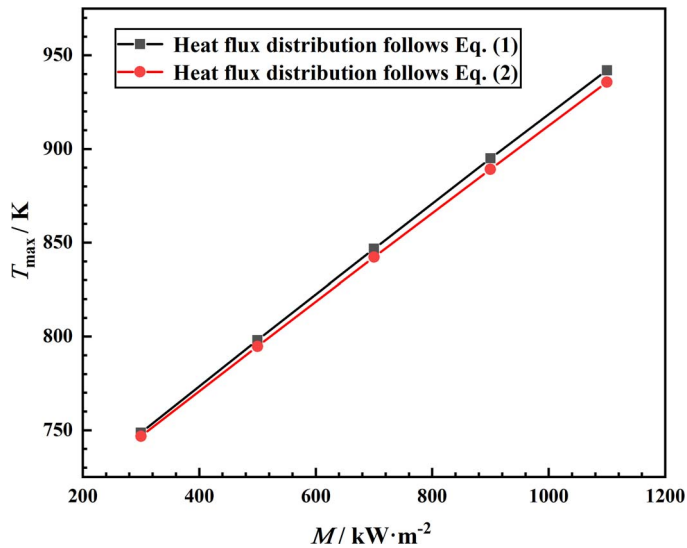**Figure 11.** *Variations of maximum temperature of the tube wall with peak heat flux M.*

equivalent stress amplitude $\sigma^{eq}_{eff\_max}$ and mean stress $\sigma^{m}_{eff\_max}$. Finally, the yearly cumulative fatigue damage D resulting from these cycles and the fatigue life L are obtained by the linear damage rule as shown in Eq. (8) and Eq. (9).

5) **Obtain the final AFD.** Repeat steps 3 to 4 until the convergence criterion of $| L - 30 | \leq \varepsilon$ is satisfied and the final AFD can be obtained.

3 RESULTS AND DISCUSSION

3.1 Model validation

Results from previous publications are used to validate the reliability of the numerical simulation results. For the molten salt flow and heat transfer validation, the heat flux is fitted according to the results of Wang *et al.* [29]. The inlet velocity and temperature of molten salt are 3 m/s and 673 K, respectively. The length and inner/outer radius of the receiver tube are, respectively, 3 m and 10.5/12.5 mm with tube material of 316 L stainless steel. Figure 7 presents the comparison of temperature distribution of the tube wall with the result of Wang *et al.* [29]. The result shows that the simulated temperature distribution of this paper is consistent with the data in literature [29] and the maximum deviation of wall temperature is 1.5%.

For the thermal stress validation, only the radial temperature gradient of the tube wall is considered. The size and material of the tube wall are the same as above. The inner and outer tube wall temperatures are, respectively, 700 K and 800 K. As shown in Figure 8, the simulated stress is compared with the result derived from the thermal stress analytic equations presented by Young *et al.* [6]. The maximum deviation between the numerical and analytic models is found to be within 5%.

3.2 Temperature and thermal stress distribution

Figure 9 and Figure 10, respectively, show the temperature distributions of the tube wall under heat flux distributions of Eq. (1) and Eq. (2) with peak heat flux M of 500 kW/m². It can be seen that the temperature distribution is more concentrated along the axis direction of the tube wall under the heat flux distribution without considering cosine effect (Eq. (1)), while the temperature distribution under the heat flux distribution considering cosine effect (Eq. (2)) is more concentrated in the circumferential direction. The reason can be attributed to the different axial and circumferential heat flux distributions. The maximum temperature of the tube wall is very close under heat flux distributions of Eq. (1) and Eq. (2) and both occur at the peak heat flux of the outer tube wall. Moreover, Figure 11 gives the variations of maximum temperature of the tube wall with incident peak heat flux M when the heat flux distribution follows Eq. (1) and Eq. (2). It shows that the maximum temperatures of the two incident heat flux distributions under different peak heat fluxes are very close and the largest difference is only 6 K. Therefore, whether the cosine effect of the circumferential heat flux distribution is considered almost has no effect on the maximum temperature of the tube wall.

Figure 12 and Figure 13, respectively, show the thermal stress distributions of the tube wall under heat flux distributions of Eq. (1) and Eq. (2) with peak heat flux M of 500 kW/m². It demonstrates that the maximum effective thermal stress locations are, respectively, at the center of the inner and outer sunward tube wall under heat flux distributions of Eq. (1) and Eq. (2). To illustrate it, Figure 14 and Figure 15, respectively, give the thermal stress distributions of the tube wall cross-section (z = 0 m) in different directions under heat flux distributions of Eq. (1) and Eq. (2) with peak heat flux M of 500 kW/m². It can be seen that the radial and circumferential stress distributions of the tube wall cross-section (z = 0 m) under the two heat flux distributions are similar, while the maximum axial stress locations are, respectively, at the center of the inner and outer sunward tube wall. And this is the reason why the thermal stress distributions under the two heat flux distributions are different. Besides, the maximum radial, axial and circumferential stresses under heat flux distribution of Eq. (1) are all higher than that under heat flux distribution of Eq. (2), which result in that the maximum effective thermal stresses of the tube wall under the two heat flux distributions are, respectively, 131 MPa and 104 MPa.

Figure 16 gives the variations of maximum effective thermal stress of the tube wall with incident peak heat flux M under the two heat flux distributions. It shows that the difference in maximum effective thermal stress between the two incident heat flux distributions is large, which is increased from 16 MPa to 59 MPa with peak heat flux. It can be concluded that the whether the cosine effect of the circumferential heat flux distribution is considered has a significant influence on the maximum effective thermal stress of the tube wall and the degree of influence increases with the peak heat flux. Consequently, it is very important to determine the heat flux distribution on the tube wall in evaluating
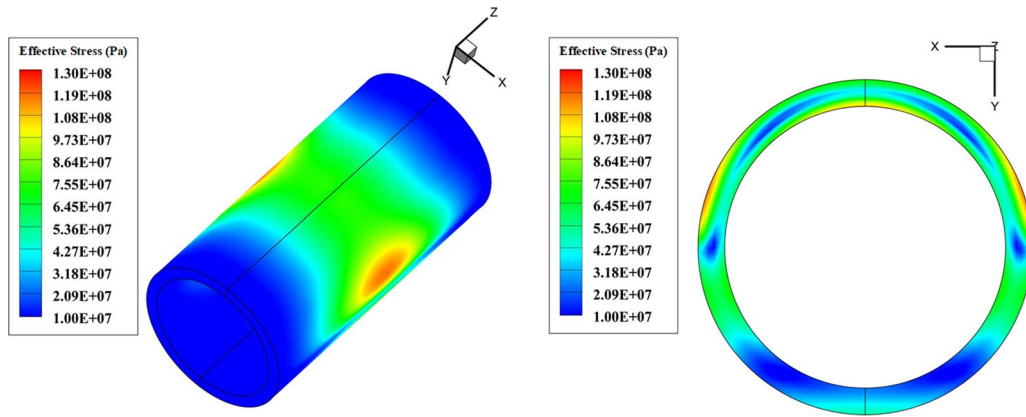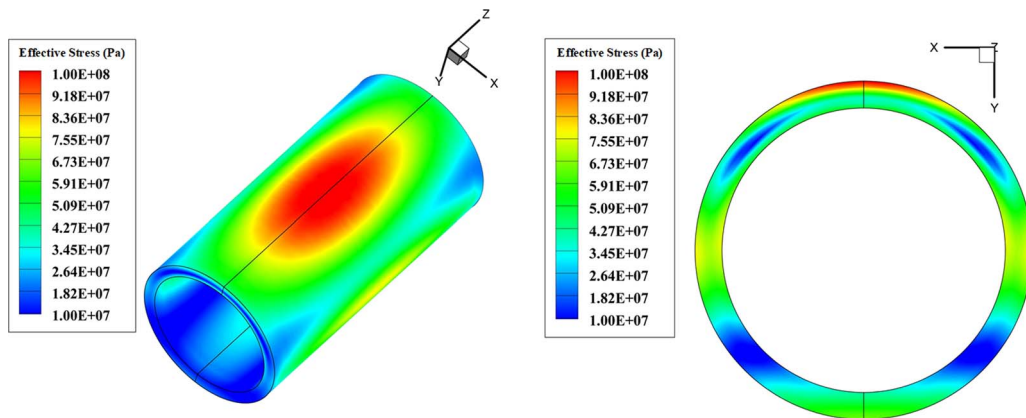
Figure 12. *Thermal stress distribution of the tube wall under heat flux distribution of Eq. (1) with peak heat flux M of 500 kW/m². (a) Whole tube wall (z = 1:60); (b) cross-wall of the tube (z = 0 m).*

Figure 13. *Thermal stress distribution of the tube wall under heat flux distribution of Eq. (2) with peak heat flux M of 500 kW/m². (a) Whole tube wall (z = 1:60); (b) cross-wall of the tube (z = 0 m).*
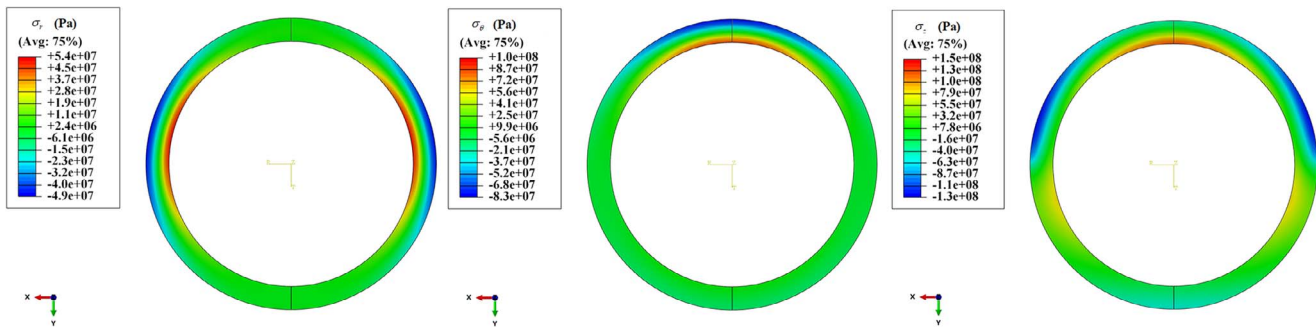

Figure 14. *Thermal stress distribution of the tube wall cross-section (z = 0 m) in different directions under heat flux distribution of Eq. (1) with peak heat flux M of 500 kW/m².*

thermal stress, which further affects the fatigue life of the receiver.

3.3 Fatigue life and AFD

Take the heat flux distribution of Eq. (1) as example, the relationship between the peak heat flux and the maximum effective thermal stress of the tube wall can be developed by Figure 16 and expressed as follows:

$$\sigma_{\text{eff\_max}} = 0.24171M + 6.22471 \ \left(R^2 = 0.99834\right) \qquad (10)$$

Once the initial value of AFD and the hourly DNI of a typical meteorological year for the site of Barstow, USA, are given,
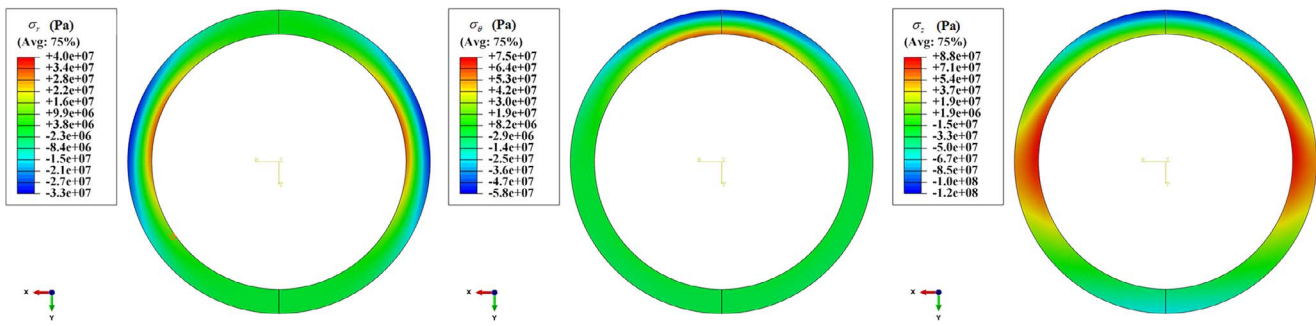
Figure 15. *Thermal stress distribution of the tube wall cross-section (z = 0 m) in different directions under heat flux distribution of Eq. (2) with peak heat flux M of 500 kW/m².*
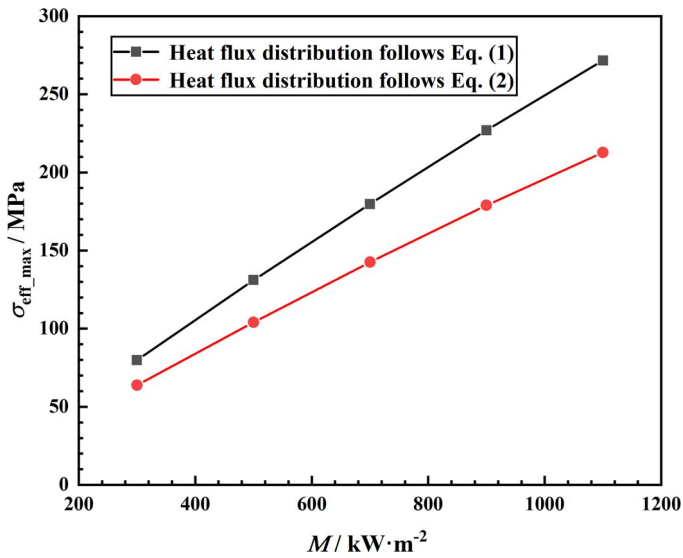

Figure 16. *Variations of maximum effective thermal stress of the tube wall with peak heat flux M.*

the hourly maximum effective thermal stress of the tube wall is obtained based on the Eq. (4) and Eq. (10). As shown in Figure 17, the hourly maximum effective thermal stress is converted into a 32 by 32 rain flow matrix and a 32 by 32 fatigue damage rate matrix of the tube wall with AFD of 900 kW/m² for the site of Barstow, USA. Comparisons of the rain flow matrix and fatigue damage rate matrix show that the fatigue damage generally occurs when the high fatigue cycle n is in the range of 10–70 and the stress amplitude $\sigma_{eff\_max}^{a}$ is high of 195–245 MPa. Based on the relationship between the stress amplitude $\sigma_{eff\_max}^{a}$ and DNI, it is obtained that the major fatigue damage of the tube wall is produced when DNI is in the range of 800–1000 W/m². Moreover, Figure 18 shows that the yearly cumulative fatigue damage and the fatigue life of the tube wall with AFD of 900 kW/m² for the site of Barstow, USA, are, respectively, 0.0266 and 18.8 years when the heat flux distribution follows Eq. (1).

The effects of heat flux distribution on the fatigue life of the tube wall are investigated under the same conditions. Figure 17b and Figure 19b present that the fatigue damage of the tube wall

is obviously higher under the heat flux distribution without considering cosine effect (Eq. (1)) than the results obtained when the cosine effect is considered (Eq. (2)). The reason is that the fatigue damage of the tube wall is the combined effects of high fatigue cycle n and high stress amplitude $\sigma_{eff\_max}^{a}$. As shown in Figure 17a and Figure 19a, although the high fatigue cycle distributions are similar under the two heat flux distributions, the corresponding stress amplitude $\sigma_{eff\_max}^{a}$ under the heat flux distribution of Eq. (1) is about 50 MPa higher than that considering cosine effect. It can be attributed to the difference in maximum thermal stress between the two incident heat fluxes as depicted in Figure 16. Consequently, the yearly cumulative fatigue damage and the fatigue life of the tube wall with AFD of 900 kW/m² for the site of Barstow, USA, are, respectively, 0.0056 and 89.3 years when the heat flux distribution follows Eq. (2). Figure 20 gives variations of fatigue life of the tube wall with AFD under the two heat flux distributions for the site of Barstow, USA. It can be seen that the whether the cosine effect of the circumferential heat flux distribution is considered has a significant influence on the fatigue life of the tube wall and the degree of influence decreases with AFD. The AFD are, respectively, 829 kW/m² and 1037 kW/m² under uniform and cosine circumferential heat flux distribution for the site of Barstow, USA, when the design lifetime of the tube is 30 years.

To investigate the effects of local weather data on the fatigue life of the tube wall, the other two SPT sites are discussed under the same conditions. Figure 17b, Figure 21b and Figure 22b show that the fatigue damage of the tube wall for the site of Barstow, USA, is the highest compared with Sevilla, Spain, and Delingha, China. It is because that both the high fatigue cycle n and the corresponding stress amplitude $\sigma_{eff\_max}^{a}$ in Sevilla, Spain, and Delingha, China, are lower than that in Barstow, USA, as demonstrated in Figure 17a, Figure 21a and Figure 22a. The corresponding stress amplitude $\sigma_{eff\_max}^{a}$ to the fatigue damage are, respectively, 195–245 MPa, 185–225 MPa and 185–260 MPa in Barstow, USA, Sevilla, Spain, and Delingha, China. Based on the relationship between the stress amplitude $\sigma_{eff\_max}^{a}$ and DNI, it can be obtained that the fatigue damage of the tube wall is produced when DNI is high of 750–1100 W/m². Therefore, it can be concluded that the more insolation hours of high DNI, the greater fatigue damage is produced. To further demonstrate it, variations
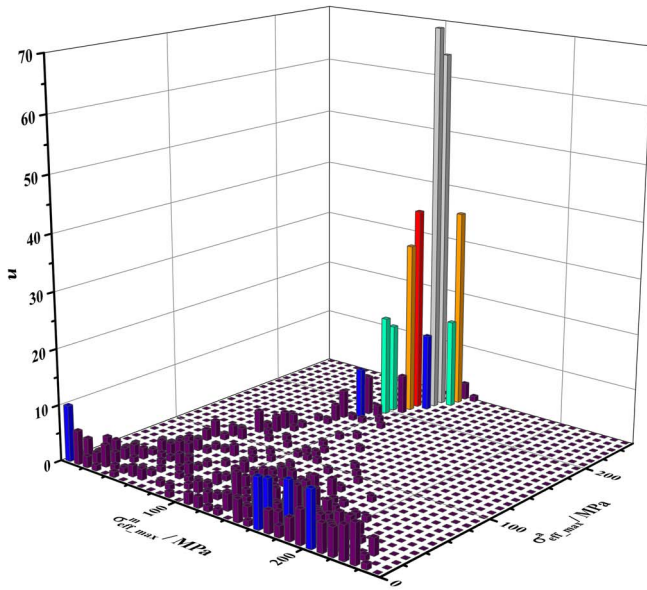
(a)
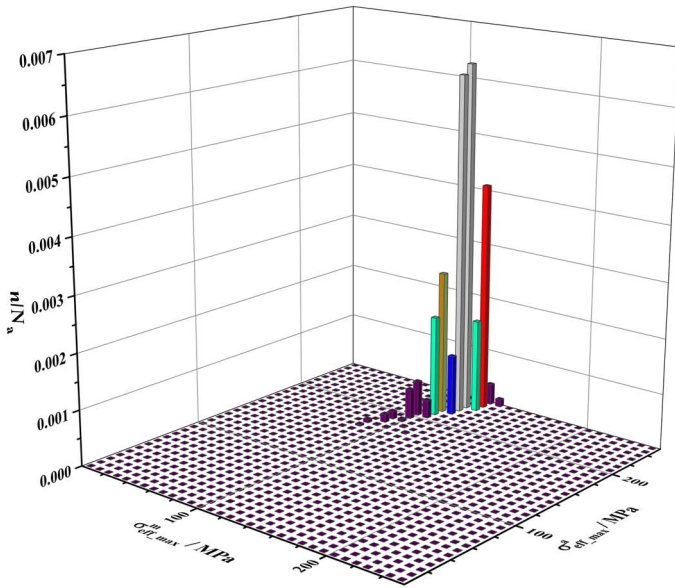
(b)

Figure 17. *Rain flow matrix and fatigue damage rate matrix of the tube wall with AFD of 900 kW/m² for the site of Barstow, USA, when the heat flux distribution follows Eq. (1). (a) Rain flow matrix; (b) fatigue damage rate matrix.*

of insolation hours with DNI range for a typical meteorological year at these three locations, which are given in Figure 4. It can be seen that the insolation hours of DNI in the range of 750–1100 W/m² for a typical meteorological year in Barstow, USA, Sevilla, Spain, and Delingha, China are, respectively, 1931, 863 and 509, which result in that the fatigue damage of the tube wall in Barstow, USA, is the greatest and the fatigue damage of the tube wall in Delingha, China, is the lowest under the same conditions. Figure 23 shows variations of fatigue life of the tube wall with AFD for different sites when the heat flux distribution follows Eq.
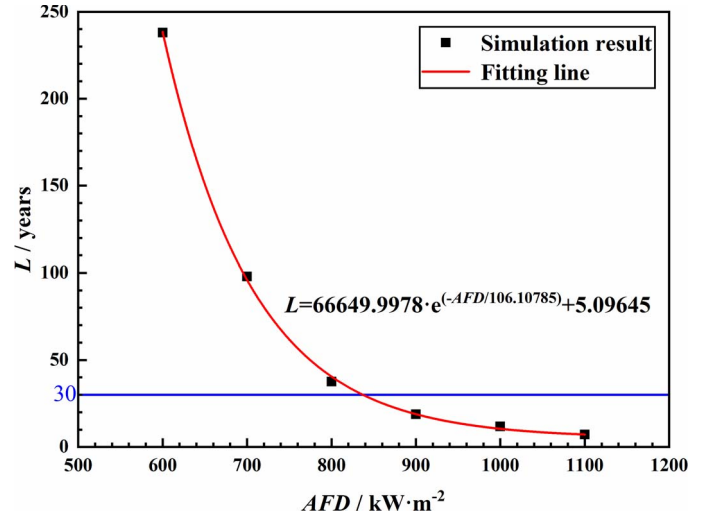

Figure 18. *Variations of fatigue life of the tube wall with AFD for the site of Barstow, USA, when the heat flux distribution follows Eq. (1).*

(1). It demonstrates that the AFD are, respectively, 829 kW/m², 973 kW/m² and 997 kW/m² for the site of Barstow, USA, Sevilla, Spain, and Delingha, China, when the design lifetime of the tube is 30 years. Consequently, the SPT site local weather has significant effects on the fatigue life and AFD design of the receiver.

4 CONCLUSIONS

In this paper, based on the coupled thermal–structural analysis and Miner linear damage theory of the SPT receiver, the relationship between the fatigue life and AFD of the tube wall is developed, allowing to investigate the effects of incident heat flux distribution and SPT site weather data on the thermal stress, fatigue life and AFD of the molten salt receiver tube. The main contributions of this work are summarized as follows,

(1) The thermal–structural analysis results show that whether the cosine effect of the circumferential heat flux distribution is considered almost has no effect on the maximum temperature of the tube wall, but it has a significant influence on the maximum thermal stress and the degree of influence increases with the peak heat flux.

(2) Due to the difference in the maximum thermal stress, the fatigue damage of the tube wall is obviously higher under the heat flux distribution without considering cosine effect (Eq. (1)) than that the cosine effect is considered (Eq. (2)), which results in that the AFD are, respectively, 829 kW/m² and 1037 kW/m² under heat flux distributions of Eq. (1) and Eq. (2) for the site of Barstow, USA, when the design lifetime of the tube is 30 years.

(3) Compared with the SPT sites of Sevilla, Spain, and Delingha, China, the fatigue damage of the tube wall in Barstow, USA, is
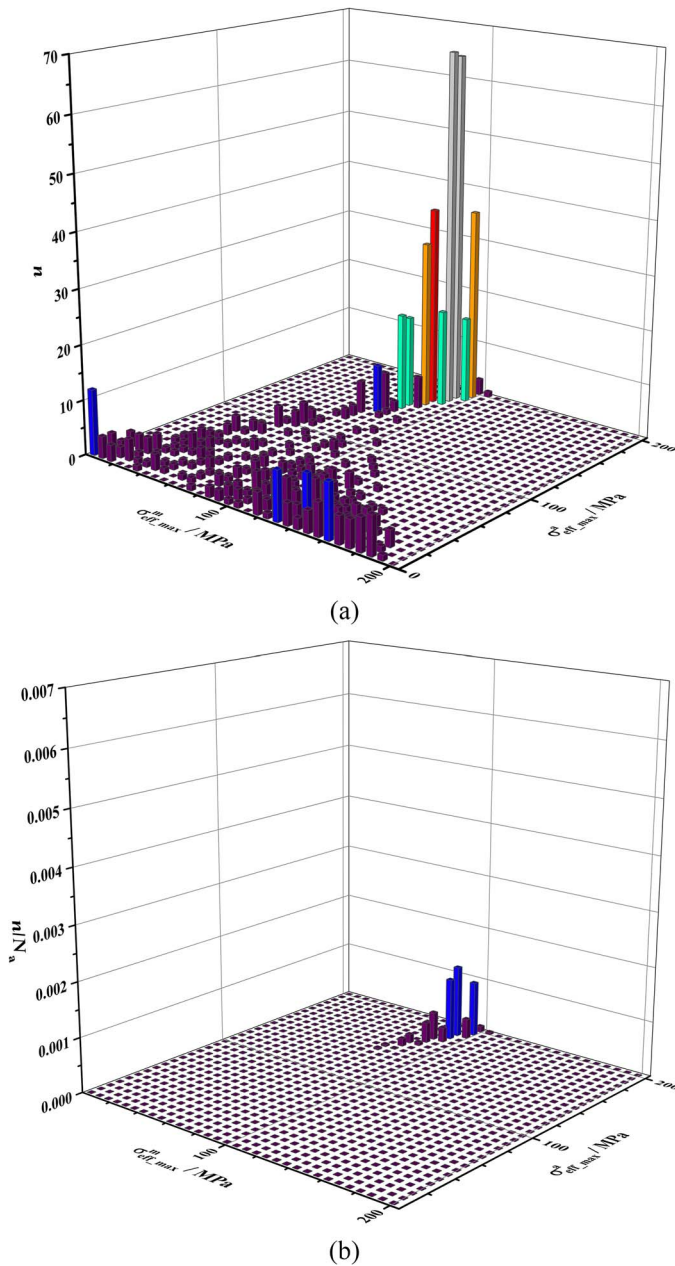
(a)

(b)

Figure 19. *Rain flow matrix and fatigue damage rate matrix of the tube wall with AFD of 900 kW/m² for the site of Barstow, USA, when the heat flux distribution follows Eq. (2). (a) Rain flow matrix; (b) fatigue damage rate matrix.*
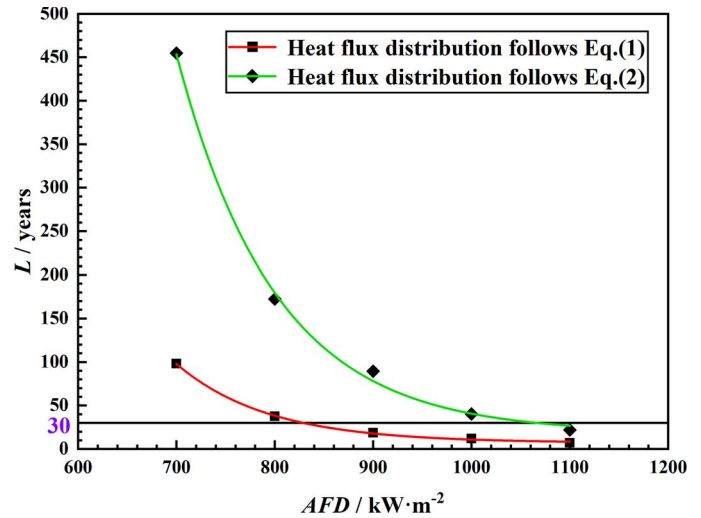

Figure 20. *Variations of fatigue life of the tube wall with AFD under different heat flux distributions for the site of Barstow, USA.*

the greatest under the same conditions due to highest insolation hours of DNI in the range of 750–1100 W/m². The AFD are, respectively, 829 kW/m², 973 kW/m² and 997 kW/m² for the site of Barstow, USA, Sevilla, Spain, and Delingha, China when the design lifetime of the tube is 30 years.

ACKNOWLEDGMENT

REFERENCES

[1] Du BC, He YL, Zheng ZJ *et al.* Analysis of thermal stress and fatigue fracture for the solar tower molten salt receiver. *Appl Therm Eng* 2016;**99**:741–50.

[2] Sánchez-González A, Rodríguez-Sánchez MR, Santana D. Aiming strategy model based on allowable flux densities for molten salt central receivers. *Sol Energy* 2017;**157**:1130–44.

[3] Sánchez-González A, Rodríguez-Sánchez MR, Santana D. Allowable solar flux densities for molten-salt receivers: input to the aiming strategy. *Results Eng* 2020;**5**. 100074.

[4] Rodríguez-Sánchez MR, Soria-Verdugo A, Almendros-Ibáñez JA *et al.* Thermal design guidelines of solar power towers. *Appl Therm Eng* 2014;**63**:428–38.

[5] Nithyanandam K, Pitchumani R. Thermal and structural investigation of tubular supercritical carbon dioxide power tower receivers. *Sol Energy* 2016;**135**:374–85.

[6] Young WC, Budynas RG, Sadegh AM. 2012. *Roark's Formulas for Stress and Strain*. New York: McGraw-Hill.

[7] Timošenko SP. 1951. *Theory of Elasticity*. New York: McGraw-Hill.

[8] Kim JS, Potter D, Gardner W *et al.* Ideal heat transfer conditions for tubular solar receivers with different design constraints. *AIP Conf. Proc.* 2017;**1850**. 030030.

[9] Conroy T, Collins MN, Fisher J, Grimes R. Levelized cost of electricity evaluation of liquid sodium receiver designs through a thermal performance, mechanical reliability, and pressure drop analysis. *Sol Energy* 2018;**166**:472–85.

[10] Ortega J, Khivsara S, Christian J *et al.* Coupled modeling of a directly heated tubular solar receiver for supercritical carbon dioxide Brayton cycle: structural and creep-fatigue evaluation. *Appl Therm Eng* 2016;**109**:979–87.

[11] Wan Z, Fang J, Tu N *et al.* Numerical study on thermal stress and cold startup induced thermal fatigue of a water/steam cavity receiver in concentrated solar power (CSP) plants. *Sol Energy* 2018;**170**:430–41.

[12] Montoya A, Rodríguez-Sánchez MR, López-Puente J, Santana D. Numerical model of solar external receiver tubes: influence of mechanical boundary conditions and temperature variation in thermoelastic stresses. *Sol Energy* 2018;**174**:912–22.
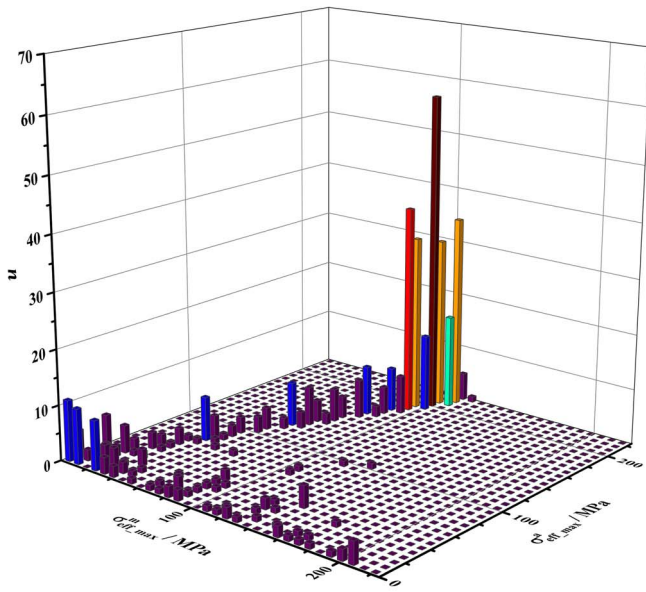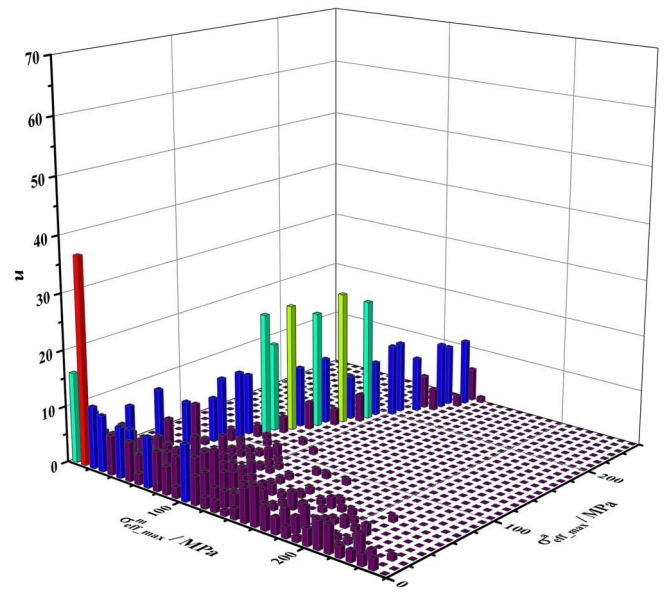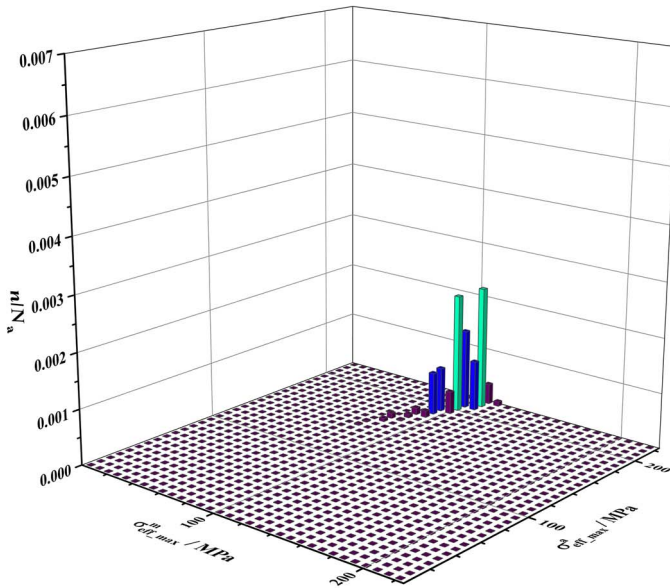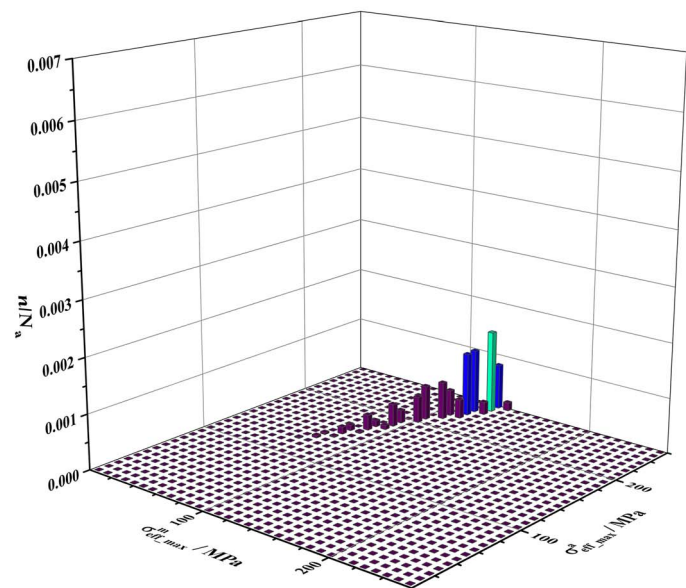
Figure 21. *Rain flow matrix and fatigue damage rate matrix of the tube wall with AFD of 900 kW/m² for the site of Sevilla, Spain, when the heat flux distribution follows Eq. (1). (a) Rain flow matrix; (b) fatigue damage rate matrix.*

Figure 22. *Rain flow matrix and fatigue damage rate matrix of the tube wall with AFD of 900 kW/m² for the site of Delingha, China, when the heat flux distribution follows Eq. (1). (a) Rain flow matrix; (b) fatigue damage rate matrix.*

[13] Wang WQ, Li MJ, Cheng ZD *et al.* Coupled optical-thermal-stress characteristics of a multi-tube external molten salt receiver for the next generation concentrating solar power. *Energy* 2021;**233**. 121110.

[14] Peng K, Qin FGF, Jiang R, Kang S. Effect of tube size on the thermal stress in concentrating solar receiver tubes. *J Sol Energy Eng* 2020;**142**. 051008.

[15] Wang F, Shuai Y, Yuan Y, Liu B. Effects of material selection on the thermal stresses of tube receiver under concentrated solar irradiation. *Mater Des* 2012;**33**:284–91.

[16] Li XL, Tang GH, Yang DL *et al.* Thermal-hydraulic-structural evaluation of S–CO2 cooling wall tubes: a thermal stress evaluating criterion and optimization. *Int J Therm Sci* 2021;**170**. 107161.

[17] Narayanan TV, Rao MSM, Carli G. Structural design and life assessment of a molten salt solar receiver. *Trans ASME* 1985;**107**:258–63.

[18] Chen Y, Zhang Y, Wang D *et al.* Effects of design parameters on fatigue–creep damage of tubular supercritical carbon dioxide power tower receivers. *Renew Energy* 2021;**176**:520–32.

[19] Neises TW, Wagner MJ, Gray AK. Structural design considerations for tubular power tower receivers operating at 650 C. *ASME 8th International Conference on Energy Sustainability* 2014.

[20] Vant-Hull LL. The role of "allowable flux density" in the design and operation of molten-salt solar central receivers. *J Sol Energy Eng* 2002;**124**:165–9.
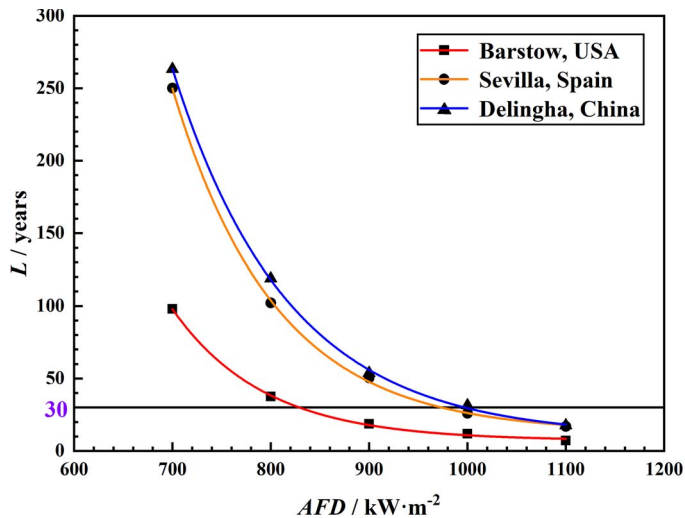
Figure 23. *Variations of fatigue life of the tube wall with AFD for different sites when the heat flux distribution follows Eq. (1).*

[21] Liao Z, Li X, Xu C *et al.* Allowable flux density on a solar central receiver. *Renew Energy* 2014;**62**:747–53.

[22] Luo Y, Du X, Yang L *et al.* Study on the allowable flux density for a solar central dual-receiver. *Energy Procedia* 2015;**69**:138–47.

[23] Kistler BL. 1987. *Fatigue Analysis of a Solar Central Receiver Design Using Measured Weather Data*. Livermore, CA: Sandia National Laboratories.

[24] Zavoico AB. 2001. *Solar Power Tower Design Basis Document*. Albuquerque, NM: Sandia National Laboratories.

[25] Boerema N, Morrison G, Taylor R, Rosengarten G. High temperature solar thermal central-receiver billboard design. *Sol Energy* 2013;**97**: 356–68.

[26] Marocco L, Cammi G, Flesch J, Wetzel T. Numerical analysis of a solar tower receiver tube operated with liquid metals. *Int J Therm Sci* 2016;**105**:22–35.

[27] Liu J, He Y, Lei X. Heat-transfer characteristics of liquid sodium in a solar receiver tube with a nonuniform heat flux. *Energies* 2019;**12**:1432.

[28] Fang J, Zhang C, Tu N *et al.* Numerical investigation on heat transfer and thermoelastic stress in a solar cavity receiver. *Appl Therm Eng* 2021;**198**. 117430.

[29] Wang JN, Li X, Chang C. Analysis of the influence factors on the overheat of molten salt receiver in solar tower power plant. *Proc CSEE* 2010;**30**: 107–14.

[30] Cheng ZD, He YL, Cui FQ *et al.* Numerical simulation of a parabolic trough solar collector with nonuniform solar flux conditions by coupling FVM and MCRT method. *Sol Energy* 2012;**86**:1770–84.

[31] Fauple JH, Fisher FE. 1981. *Engineering Design—A Synthesis of Stress Analysis and Material Engineering*. New York: Wiley.

[32] Conroy T, Collins MN, Fisher J, Grimes R. Thermal and mechanical analysis of a sodium-cooled solar receiver operating under a novel heliostat aiming point strategy. *Appl Energy* 2018;**230**:590–614.

[33] Fernández-Torrijos M, González-Gómez PA, Sobrino C, Santana D. Economic and thermo-mechanical design of tubular sCO2 central-receivers. *Renew Energy* 2021;**177**:1087–101.

[34] Kolb GJ. 2011. *An Evaluation of Possible Next-Generation High-Temperature Molten-Salt Power Towers*. Albuquerque, NM: Sandia National Laboratories.

[35] System Advisor Model (SAM), version 2017.9. 5.

[36] Xu C, Wang Z, Li X, Sun F. Energy and exergy analysis of solar power tower plants. *Appl Therm Eng* 2011;**31**:3904–13.

[37] Amzallag C, Gerey JP, Robert JL *et al.* Standardization of the rainflow counting method for fatigue analysis. *Int J Fatigue* 1994;**16**:287–93.

[38] Dowling NE. Mean stress effects in stress-life and strain-life fatigue. *SAE Technical Paper* 2004;**32**:1004–19.

[39] ASME. ASME Boiler & Pressure Vessel Code, Section III, Subsection NH. 2007. *Class 1 Components in Elevated Temperature Service*. Fairfield, NJ: The American Society of Mechanical Engineers.

[40] Ellyin F. 2012. *Fatigue Damage, Crack Growth and Life Prediction*. Berlin: Springer Science & Business Media.